

Article

An Approach to Predict Geometrically and Thermo-Mechanically Induced Stress Concentrations in Ribbed Reinforcing Bars

Tobias Robl ^{1,*}, Christoph Hubertus Wölfle ¹, Muhammed Zubair Shahul Hameed ¹, Stefan Rapp ²,
Christian Krempaszky ¹ and Ewald Werner ¹

¹ Department of Materials Engineering, Institute of Materials Science and Mechanics of Materials, TUM School of Engineering and Design, Technical University of Munich, 85748 Garching, Germany; christoph.woelfle@tum.de (C.H.W.); zubair.shahul-hameed@tum.de (M.Z.S.H.); krempaszky@tum.de (C.K.); ewald.werner@tum.de (E.W.)

² Centre for Building Materials, Department of Materials Engineering, TUM School of Engineering and Design, Technical University of Munich, 81245 Munich, Germany; stefan.rappl@tum.de

* Correspondence: tobias.robl@tum.de

Abstract: Ribbed reinforcing steel bars (rebars) are used for the reinforcement of concrete structures. In service, they are subjected to cyclic loading. Several studies addressing the relationship between rib geometry, stresses at the rebar surface induced by service loads and the rebar fatigue performance can be found in literature. However, the rebar's fatigue performance is also influenced by residual stresses originating from the manufacturing process. In this contribution, a modeling approach is proposed to examine geometrically and thermo-mechanically induced stress concentrations in ribbed reinforcing bars made of the steel grade B500B. A linear-elastic load stress analysis and a thermo-mechanical analysis of the manufacturing process are conducted. The results are discussed and compared to literature results. In case of the load stress analysis, the results agree well with findings reported in literature and extend the current state of knowledge for B500B rebars with small diameters. In case of the thermo-mechanical analysis, compressive residual stresses at the rebar surface between two ribs and tensile residual stresses in the longitudinal direction at the tip of the ribs can be reported.

Keywords: reinforcing steel; manufacturing process; stress concentration; residual stresses; constitutive modeling



Citation: Robl, T.; Wölfle, C.H.; Shahul Hameed, M.Z.; Rapp, S.; Krempaszky, C.; Werner, E. An Approach to Predict Geometrically and Thermo-Mechanically Induced Stress Concentrations in Ribbed Reinforcing Bars. *Metals* **2022**, *12*, 411. <https://doi.org/10.3390/met12030411>

Academic Editors: Matteo Benedetti and Luis Reis

Received: 29 October 2021

Accepted: 22 February 2022

Published: 26 February 2022

Publisher's Note: MDPI stays neutral with regard to jurisdictional claims in published maps and institutional affiliations.



Copyright: © 2022 by the authors. Licensee MDPI, Basel, Switzerland. This article is an open access article distributed under the terms and conditions of the Creative Commons Attribution (CC BY) license (<https://creativecommons.org/licenses/by/4.0/>).

1. Introduction

Reinforcing bars are cylindrical steel bars used for the reinforcement of concrete structures [1]. Typical diameters vary from 6 to 40 mm [2]. While concrete has excellent properties with regard to loading under compression, steel is a suitable material to bear high tensile loads. The advantage of the composite structure is the ability to absorb both high compressive and high tensile loads.

Rebars are made from low-carbon steels with a carbon content of approx. 0.2 wt% [3]. A typical manufacturing route is the so called TempCoreTM process (Figure 1), within which the rebar is rapidly quenched from the austenitic state by water spray cooling in a first step after hot-rolling. During this first step, the outer layer of the rebar transforms from austenite to martensite and possibly bainite up to a certain hardening depth, while the core stays austenitic. In a second step, the rebar is cooled to room temperature in air. During this second step, the remaining austenite transforms into ferrite and pearlite while the heat from the core reheats the outer martensitic layer, which becomes tempered (Figure 2). By adjusting the heat treatment, the TempCoreTM process allows to produce rebars of different strength and high ductility without the need for expensive alloying elements [4,5].

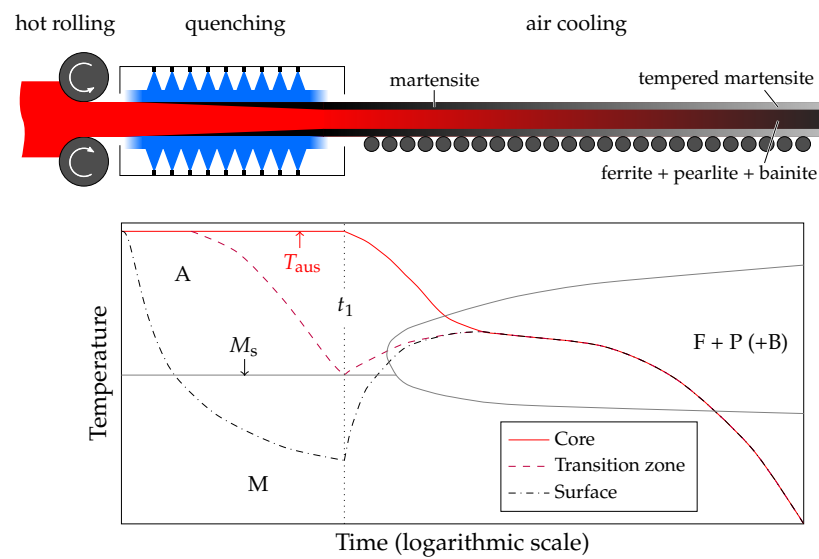
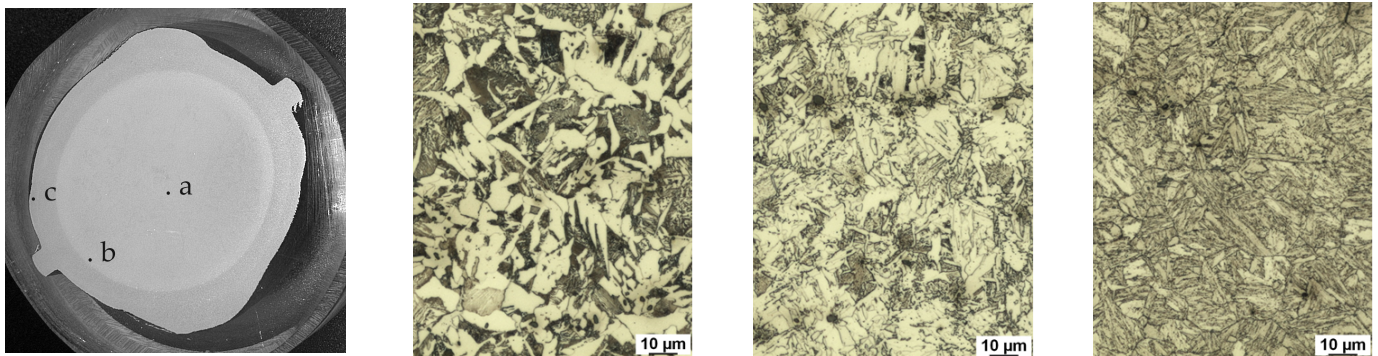


Figure 1. Schematic representation of the TempCore™ process (austenite, A; martensite, M; ferrite, F; pearlite, P; bainite, B; martensite start temperature, M_s ; austenitization temperature, T_{aus} ; and quenching time, t_1) [3].



Cross-section of the rebar (positions of the micrographs indicated).

(a) Ferritic-pearlitic core.

(b) Bainitic transition zone.

(c) Tempered martensite close to the surface.

Figure 2. Microstructure variations within the cross-section of a B500B steel rebar with a diameter of 28 mm [3].

The development of modern rebars advanced in the 1960s and 1970s. In this course, different surface geometries, such as transverse ribs, were introduced. These ribs allow the transmission of loading stresses between rebar and concrete along the whole length of the bar [6–9]. However, ribs lower the fatigue performance of the reinforcement, as they lead to high stress concentrations at the rebar surface.

Several studies addressing the relationship between rib geometry, stresses at the rebar surface induced by service loads and the rebar fatigue performance have been conducted [10–24]. The rib volume and the foot radius of the transverse rib were identified to have the main impact on the rebar fatigue performance.

However, the rebar's fatigue performance is also influenced by residual stresses originating from the manufacturing process due to the asynchronous shrinkage of the surface and the core regions as well as the transformation strain accompanying the decomposition of austenite [25]. Residual and loading stresses are superimposed in service. As a consequence, tensile residual stresses at the rebar surface potentially result in earlier failure of the reinforcement, while compressive residual stresses favor a prolonged service life [26].

However, a targeted formation of compressive residual stresses at the rebar surface is not well understood.

Due to the complex rebar geometry, it is difficult to completely determine the stress state in service as well as the residual stress state present after heat treatment by experimental investigations [27]. Experimental approaches to determine residual stresses are restricted to single stress components or to the rebar surface [3,17,18,26,28]. To close this gap, numerical simulation plays an important role. In order to examine the stress state in service by means of finite element simulations, it is necessary to properly describe the rebar geometry, the manufacturing process and the material behavior. As the thermal and mechanical material behavior depend on the local phase composition, it is also important to determine the corresponding, phase-specific material parameters and to describe the relevant phase transformations.

Recent modeling approaches [29–36] to examine the TempCore™ process thus far are restricted to the analysis of the heat conduction problem and the microstructural evolution as well as to unribbed rebars. The mechanical properties at room temperature are predicted based on the phase fractions of the constituting phases and the phase properties. To the best knowledge of the authors, a numerical prediction of residual stresses in ribbed rebars has not yet been carried out.

In this contribution, a modeling approach to predict geometrically and thermo-mechanically induced stress concentrations in ribbed reinforcing bars is proposed. To solve the boundary value problems considered, the commercial finite element code ABAQUS is used [37]. A load stress analysis and a thermo-mechanical analysis of the manufacturing process are carried out. The numerical predictions are discussed and compared to literature results.

2. Modeling

The investigations in this study were conducted for the B500B reinforcement steel grade (material number 1.0439 according to DIN EN ISO 17660 [38]), which is the most common rebar grade in the German market. Rebars made from B500B are characterized by two or four rows of transverse ribs and exhibit none or two longitudinal ribs [1,2]. To capture the rebar geometry (Figure 3) in the load stress analysis, a periodic unit cell according to Figure 4 was used. To study the residual stress distribution at the rebar surface in case of the thermo-mechanical analysis, the use of submodeling techniques is necessary (Figure 5b). The boundary conditions for the submodel are prescribed by a global model, i.e., the periodic unit cell (Figure 5a).

2.1. Geometry

For this study, an idealized geometry with two rows of transverse and two longitudinal ribs was used. The model geometry was generated according to the specifications given in Table 1 using the 3D-CAD-programm SOLID WORKS [39], see also Figure 3a–c. However, by analyzing an idealized geometry, micro- and mesoscopic surface properties, such as defects and surface roughness, are neglected. This simplification was considered permissible, as the impact of micro- and mesoscopic surface properties on the fatigue behavior is reported to be of minor importance. Burton [11] conducted fatigue tests on reinforcing bars. The reinforcing bars were either produced by new, partially worn or fully worn rolls and, therefore, exhibited a different surface roughness. The test results indicated, however, that all three types of reinforcing bars showed a similar fatigue performance. Martin et al. [19] conducted fatigue tests on reinforcing bars with ribbed surfaces as well as on cylindrical bars with turned and rolled surfaces, respectively. While the fatigue performance of the cylindrical bars was similar, the fatigue performance of the ribbed reinforcing bars decreased.

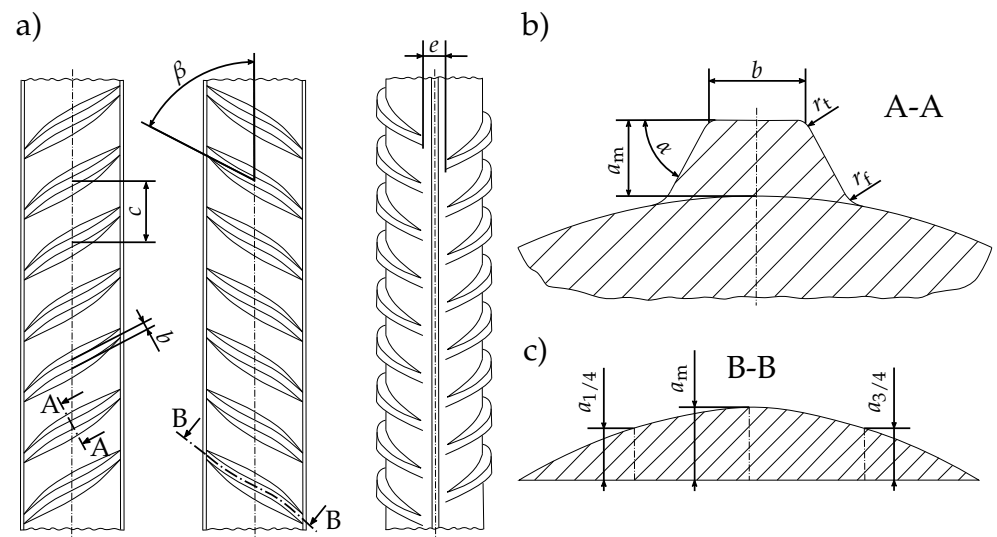


Figure 3. Idealized geometry of B500B rebar steel grade with longitudinal ribs according to DIN-488-2 [2]: (a) overall view, (b) cross section transverse rib and (c) longitudinal section transverse rib.

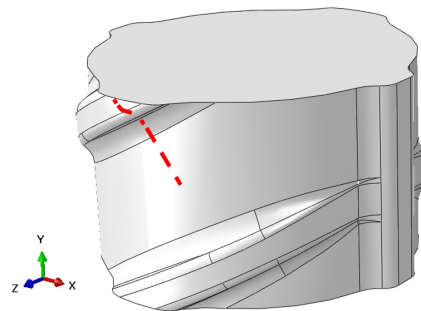


Figure 4. Periodic unit cell used for the load stress analysis (path for evaluation highlighted in red).

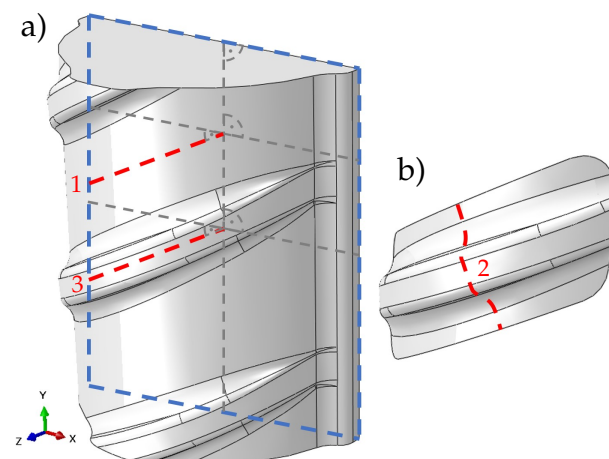


Figure 5. Periodic unit cell (a) and submodel (b) used for the thermo-mechanical analysis (paths for evaluation highlighted in red, symmetry plane highlighted in blue).

2.2. Load Stress Analysis

To discretize the rebar geometry, C3D10 elements were used [37]. As the service loads remain below the rebar's yield strength of at least 500 MPa, a linear-elastic material behavior was applied, where Young's modulus and Poisson's ratio were assumed as $E = 200$ GPa and $\nu = 0.3$, which are typical values for steel. Periodic boundary conditions

enforce a congruent deformation of the top and bottom surfaces. As rebars are loaded predominantly in tension [27], the engineering strain

$$\varepsilon_y = \frac{u_y}{c} = \frac{\sigma_y}{E} \quad (1)$$

is applied to the unit cell via the master node displacement

$$u_y = \varepsilon_y \cdot c = \frac{\sigma_y}{E} \cdot c \quad (2)$$

in the axial direction y . c is the rib spacing and σ_y is the loading stress in the axial direction of the unit cell. For the numerical analysis, the loading stress was freely chosen. To evaluate the computational results, the maximum ratio of the von Mises equivalent stress, $\sigma_{vM_{max}}$, and the loading stress, σ_y , was identified along the path shown in Figure 4.

Table 1. Parameter set following DIN 488-2 [2] to specify the rebar model geometry.

Rebar	Symbol	Reference Value	Unit
Rebar diameter ⁽¹⁾	d	12.00	mm
Bar diameter ⁽²⁾	d_{bar}	11.70	mm
Transverse Ribs	Symbol	Reference Value	Unit
Distance between rib rows	e	2.00	mm
Rib spacing	c	7.20	mm
Foot radius	r_f	0.80	mm
Tip radius	r_t	0.36	mm
Rib width	b	1.20	mm
Rib height (middle of the rib)	a_m	0.78	mm
Rib height (one-/three-quarter point)	$a_{1/4}, a_{3/4}$	0.54	mm
Flank inclination	α	65	°
Rib inclination	β	60	°
Longitudinal Ribs	Symbol	Reference Value	Unit
Foot radius	$r_{f,l}$	1.00	mm
Tip radius	$r_{t,l}$	0.60	mm
Rib width	b_l	2.00	mm
Rib height	a_l	0.60	mm
Flank inclination	α_l	90	°

⁽¹⁾ weight-specific diameter ⁽²⁾ diameter of the base cylinder, see DIN 488-2 [2].

2.3. Thermo-Mechanical Analysis

Within the thermo-mechanical analysis, the thermal and the mechanical problems are solved on the global level as well as on the submodel level. To solve the thermal and the mechanical problem, a sequential approach was chosen. This is reasonable if the plastic deformation of the rebar is small, as in the present case (cf. Figure A2d), where the mechanical problem is independent from the thermal one as well as from the microstructural evolution. DC3D4 and C3D4 elements are used to discretize the rebar geometry in case of the thermal and the mechanical analysis, respectively [37].

In addition to the periodic boundary conditions, which ensure consistent temperature and displacement fields at the top and bottom surfaces of the unit cell, a symmetry boundary condition was applied to the symmetry plane of the unit cell. To describe the thermo-mechanical material behavior with respect to the local phase fractions, the user subroutines UMATHT, UHARD and UEXPAN are used [37]. While the user subroutine UMATHT was utilized to define the thermal constitutive behavior of the material, the user subroutine UHARD was utilized to define the plastic material behavior. In order to specify the incremental thermal strains as a function of temperature and the local phase fractions, the user subroutine UEXPAN was employed.

Within the model, the decomposition of austenite into martensite and into the phases formed predominantly by diffusional decomposition of austenite, i.e., bainite, pearlite and ferrite, was considered. The tempering of martensite was neglected as well as transformation plasticity [40,41]. The full parameter-set to describe the thermo-mechanical material behavior and the microstructural evolution is given in Tables 2 and 3 as well as in Figure 6.

Table 2. Parameter values to describe the phase-specific, thermo-mechanical material behavior: Temperature, T , thermal conductivity, λ_i , specific heat capacity, $c_{p,i}$, density, ρ_i , Young's modulus, E_i , Poisson's ratio, ν_i , yield stress, Y_i , starting parameter to determine thermal expansion according to Equation (18), $\varepsilon_i^{\text{th}}(T = 0^\circ\text{C})$, and linear thermal expansion, α_i .

$T [^\circ\text{C}]$	$\lambda_{\text{aus}} [\text{W/mK}]^{(1)}$	$\lambda_{\text{mar}} [\text{W/mK}]^{(1)}$	$\lambda_{\text{bpf}} [\text{W/mK}]^{(1)}$
0	16.75	54.43	54.53
300	20.93	43.96	43.96
600	25.12	37.68	37.68
900	29.31	29.31	29.31
$T [^\circ\text{C}]$	$c_{p,\text{aus}} \cdot \rho_{\text{aus}} [\text{MJ/Km}^3]^{(1)}$	$c_{p,\text{mar}} \cdot \rho_{\text{mar}} [\text{MJ/Km}^3]^{(1)}$	$c_{p,\text{bpf}} \cdot \rho_{\text{bpf}} [\text{MJ/Km}^3]^{(1)}$
0	3.18	3.52	3.52
300	3.60	3.85	3.85
600	3.98	4.27	4.27
900	4.40	4.61	4.61
$T [^\circ\text{C}]$	$E_{\text{aus}} [\text{GPa}]^{(2)}$	$E_{\text{mar}} [\text{GPa}]^{(2)}$	$E_{\text{bpf}} [\text{GPa}]^{(2)}$
0	-	210	210
200	195	195	195
300	188	188	188
600	160	160	160
714	140	-	140
820	107	-	107
900	107	-	-
$T [^\circ\text{C}]$	$\nu_{\text{aus}} [-]^{(3)}$	$\nu_{\text{mar}} [-]^{(3)}$	$\nu_{\text{bpf}} [-]^{(3)}$
0–900	0.3	0.3	0.3
$T [^\circ\text{C}]$	$Y_{\text{aus}} [\text{MPa}]^{(4)}$	$Y_{\text{mar}} [\text{MPa}]^{(4)}$	$Y_{\text{bpf}} [\text{MPa}]^{(6)}$
0	-	1315	440
200	125 ⁽⁵⁾	1065	349
300	121 ⁽⁵⁾	940	322
600	103 ⁽⁵⁾	280	96
714	90	-	84 ⁽⁷⁾
820	75	-	64 ⁽⁷⁾
900	37	-	-
$T [^\circ\text{C}]$	$\varepsilon_{\text{aus}}^{\text{th}}(T = 0^\circ\text{C}) [-]^{(8)}$	$\varepsilon_{\text{mar}}^{\text{th}}(T = 0^\circ\text{C}) [-]^{(8)}$	$\varepsilon_{\text{bpf}}^{\text{th}}(T = 0^\circ\text{C}) [-]^{(8)}$
0–900	0	0.0098	0.0081
$T [^\circ\text{C}]$	$\alpha_{\text{aus}} [1/\text{K}]^{(3,8)}$	$\alpha_{\text{mar}} [1/\text{K}]^{(3,8)}$	$\alpha_{\text{bpf}} [1/\text{K}]^{(3,8)}$
0–900	$23.4 \cdot 10^{-6}$	$13.7 \cdot 10^{-6}$	$16.6 \cdot 10^{-6}$

⁽¹⁾ Phase specific values for C17 rebar steel grade [29]. ⁽²⁾ Values for B500B rebar steel grade [3]. ⁽³⁾ Assumed to be constant. ⁽⁴⁾ Phase specific values for B500B rebar steel grade [3]. ⁽⁵⁾ Extrapolated following $Y_{\text{aus}} = E_{\text{aus}}(T)/E_{\text{aus}}(714^\circ\text{C}) \cdot Y_{\text{aus}}(714^\circ\text{C})$. ⁽⁶⁾ Phase specific values for B500B rebar steel grade [42]. ⁽⁷⁾ Extrapolated following $Y_{\text{bpf}} = E_{\text{bpf}}(T)/E_{\text{bpf}}(600^\circ\text{C}) \cdot Y_{\text{bpf}}(600^\circ\text{C})$. ⁽⁸⁾ Determined by dilatometry for B500B rebar steel grade.

Table 3. Parameter values to describe the microstructural evolution: Austenite start temperature, A_{c1} , austenite finish temperature, A_{c3} , maximum phase fraction of proeutectoid ferrite, z_{\max} , martensite start temperature, M_S , rate parameter of the martensitic transformation, α_M , critical cooling rate of martensite, \dot{T}_{mar} , Avrami exponent, η , kinetic rate constants, κ_0 , κ_1 and κ_2 , and critical cooling rate of bainite, pearlite and ferrite, \dot{T}_{bpf} .

B500B			Martensite				Bainite/Pearlite/Ferrite				
A_{c1} [°C]	A_{c3} [°C]	z_{\max} [-]	M_S [°C]	α_M [K ⁻¹]	\dot{T}_{mar} [Ks ⁻¹]	η [-]	κ_0 [-]	κ_1 [K ⁻¹]	κ_2 [K ⁻²]	\dot{T}_{bpf} [Ks ⁻¹]	
714 ⁽¹⁾	820 ⁽¹⁾	0.75 ⁽²⁾	420 ⁽¹⁾	0.021 ⁽¹⁾	-60 ⁽¹⁾	1 ⁽³⁾	13.2 ⁽³⁾	0.0529 ⁽³⁾	-5.01·10 ⁻⁵ ⁽³⁾	-190 ⁽⁴⁾	

⁽¹⁾ Determined with JMatPro [43] for B500 rebar grade with chemical composition according to [3]. ⁽²⁾ Determined from the iron-carbon phase-diagram according to the lever rule for a steel with a carbon content of 0.2%. ⁽³⁾ Determined by least squares regression based on the CCT- and the TTT-diagram of B500B rebar steel (CCT- and TTT- diagram generated with JMatPro [43] for B500B rebar grade with chemical composition according to [3]). ⁽⁴⁾ According to the CCT-diagram cited by [3] for B500B rebar steel grade.

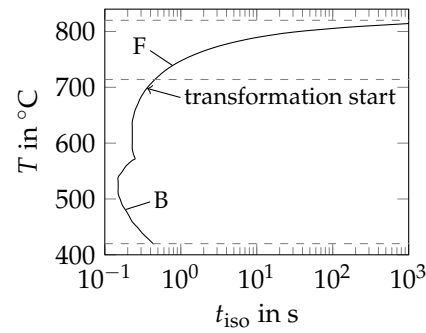


Figure 6. Transformation start, t_{iso} , for different temperatures, T , and for isothermal temperature control [43].

2.3.1. Thermal Problem

Within the thermo-mechanical analysis, the TempCoreTM process is modeled as follows: During the quenching step, a large heat transfer coefficient, h_1 , is applied at the surface of the rebar for a short period of time, $0 < t \leq t_1$. Within the air cooling step, $t_1 < t \leq t_2$, the rebar is cooled to ambient temperature, T_∞ . The heat transfer coefficient, h_2 , is small and the cooling time is large (Table 4). For axisymmetric, cylindrical bodies, the associated heat transfer problem is given as

$$\frac{\partial}{\partial r} \left(\lambda \cdot \frac{\partial T}{\partial r} \right) + \frac{\lambda}{r} \cdot \left(\frac{\partial T}{\partial r} \right) = \rho \cdot c_p \cdot \frac{\partial T}{\partial t}. \quad (3)$$

The heat transfer problem is considered to be one-dimensional with respect to the coordinate in the radial direction, r , because internal heat generation, e.g., due to latent heat associated with phase transformations or plastic dissipation, and heat flow in axial direction are neglected. T denotes the temperature, ρ the density, λ the thermal conductivity and c_p the specific heat capacity of the material. The boundary conditions at the cylinder axis,

$$\frac{\partial T}{\partial r} = 0, \quad t \geq 0, \quad r = 0, \quad (4)$$

and at the cylinder surface,

$$-\lambda \cdot \frac{\partial T}{\partial r} = h_i \cdot (T - T_\infty), \quad t > 0, \quad r = D/2, \quad (5)$$

as well as the initial condition,

$$T = T_0, \quad t = 0, \quad 0 \leq r \leq D/2, \quad (6)$$

are given with respect to the diameter of the cylinder, D , the initial temperature, T_0 , the ambient temperature, T_∞ , and the heat transfer coefficients h_1 for $0 < t \leq t_1$ and h_2 for $t_1 < t \leq t_2$ [44,45]. The ambient temperature also corresponds to the coolant temperature during the quenching step. For the numerical study, the idealized model rebar geometry is considered instead of the axisymmetric and cylindrical body (Section 2.1). The thermal conductivity,

$$\lambda = \lambda_{\text{aus}} \cdot z_{\text{aus}} + \lambda_{\text{mar}} \cdot z_{\text{mar}} + \lambda_{\text{bpf}} \cdot z_{\text{bpf}}, \quad (7)$$

and the specific heat capacity,

$$c_p = c_{p,\text{aus}} \cdot z_{\text{aus}} + c_{p,\text{mar}} \cdot z_{\text{mar}} + c_{p,\text{bpf}} \cdot z_{\text{bpf}}, \quad (8)$$

are determined by using the linear rule of mixture. Hence, both parameters depend on the phase specific thermal conductivity, λ_i , the phase specific specific heat capacity, $c_{p,i}$, and the fractions of the constituting phases, z_i . In addition to austenite, z_{aus} , and martensite, z_{mar} , this is the mixture consisting of bainite, pearlite and ferrite, z_{bpf} .

Table 4. Reference parameters for the TempCore™ process according to [4,5,30,45].

T_0 [°C]	T_∞ [°C]	t_1 [s]	t_2 [s]	h_1 [W/m ² K]	h_2 [W/m ² K]
900	20	0.4	3000	25,000 ⁽¹⁾	40

⁽¹⁾ Chosen to ensure reasonable martensite phase fractions after quenching.

2.3.2. Microstructural Evolution

While the austenite fraction,

$$z_{\text{aus}} = 1 - z_{\text{mar}} - z_{\text{bpf}}, \quad (9)$$

is determined as the remaining phase fraction, the martensite fraction,

$$z_{\text{mar}} = (1 - z_{\text{bpf}}) \cdot \left\{ 1 - \exp[-\alpha_M \cdot (M_S - T)] \right\}, \quad (10)$$

is determined according to the Koistinen–Marburger model [46], whereas the maximum martensite fraction, $z_{\text{mar,max}} = 1 - z_{\text{bpf}}$, depends on the current fraction of bainite, pearlite and ferrite. The rate parameter of the martensitic transformation is represented by α_M , the martensite start temperature by M_S . Equation (10) is evaluated for temperatures lower than the martensite start temperature, $T < M_S$, and for cooling rates below the critical cooling rate, $\dot{T} < \dot{T}_{\text{mar}}$. To ensure rising martensite fractions only, the following constraint is applied:

$$z_{\text{mar}}(t) = \max[z_{\text{mar}}(0), z_{\text{mar}}(t)]. \quad (11)$$

To determine the phase fraction of bainite, pearlite and ferrite, z_{bpf} , according to the JMAK model [47–50], the considered cooling curve has to be converted into a step curve consisting of m isothermal steps. The phase fraction after the n -th step,

$$z_{\text{bpf}}|_n = \sum_{k=1}^n (\Delta t \cdot \dot{z}_{\text{bpf}})_k, \quad 1 \leq n \leq m, \quad (12)$$

can then be determined using Scheil's additivity rule [51]. Therefore, the time increment, Δt , and the derivative of z_{bpf} with respect to time, \dot{z}_{bpf} , have to be identified for each step. According to [52], the derivative is given by

$$\dot{z}_{\text{bpf}} = (z_{\text{iso}} - z_{\text{bpf}}) \cdot \eta \cdot \kappa^{\frac{1}{\eta}} \cdot \left[-\ln \left(1 - \frac{z_{\text{bpf}}}{z_{\text{iso}}} \right) \right]^{1 - \frac{1}{\eta}} \quad (13)$$

if the mixture of bainite, pearlite and ferrite is the only product phase for a considered cooling path. To depict both the decomposition of austenite into martensite as well as into bainite, pearlite and ferrite, it is reasonable to correlate \dot{z}_{bpf} with the remaining austenite fraction,

$$\dot{z}_{\text{bpf}} = z_{\text{aus}} \cdot \dot{z}_{\text{bpf}}. \quad (14)$$

In Equation (13), the Avrami exponent and the kinetic rate constant of the JMAK model are represented by η and $\kappa = \exp(\kappa_0 + \kappa_1 \cdot T + \kappa_2 \cdot T^2)$ [29]. The maximum phase fraction of bainite, pearlite and ferrite for complete isothermal phase transformations is given as $z_{\text{iso}} = 1$ between the martensite start temperature and the austenite start temperature, $M_S \leq T \leq A_{C1}$. Between the austenite start temperature and the austenite finish temperature, $A_{C1} < T \leq A_{C3}$, the maximum phase fraction,

$$z_{\text{iso}} = z_{\text{max}} \cdot \frac{A_{C3} - T}{A_{C3} - A_{C1}}, \quad (15)$$

is determined according to the lever rule [53]. The maximum fraction of proeutectoid ferrite formed for a given carbon content, is given by z_{max} . Equation (14) is evaluated for $M_S \leq T \leq A_{C3}$, for cooling rates higher than the critical cooling rate, $\dot{T} > \dot{T}_{\text{bpf}}$, and if the transformation of bainite, pearlite and ferrite has started. For isothermal temperature control, transformation starts if $t = t_{\text{iso}}(T)$ applies, where $t_{\text{iso}}(T)$ is defined by the TTT-diagram (Figure 6). For an arbitrary cooling curve, transformation starts if

$$\sum_{k=1}^n \left(\frac{\Delta t}{t_{\text{iso}}} \right)_k \geq 1. \quad (16)$$

The volume change resulting from the transformation of austenite to martensite as well as to bainite, pearlite and ferrite, respectively, is described by:

$$\Delta \varepsilon_{\text{aus} \rightarrow i} = \Delta z_i \cdot \left[\varepsilon_i^{\text{th}}(T + \Delta T) - \varepsilon_{\text{aus}}^{\text{th}}(T + \Delta T) \right], \quad (17)$$

where i denotes martensite, bainite, pearlite and ferrite. The eigenstrain increments, $\Delta \varepsilon_{\text{aus} \rightarrow i}$, depend on the thermal strains of the individual phases,

$$\varepsilon_i^{\text{th}}(T + \Delta T) = \varepsilon_i^{\text{th}}(T = 0^\circ \text{C}) + \alpha_i \cdot (T + \Delta T), \quad (18)$$

as well as on the phase fractions, Δz_i , which are formed within the time increment, Δt , associated with the temperature decrement, ΔT .

2.3.3. Mechanical Problem

The mechanical material behavior is modeled as isotropic, thermoelastic-idealplastic. The von Mises yield criterion and the associated flow rule are used to describe the plastic material behavior [54]. Using the linear rule of mixture, which is a common modeling approach with regard to quench hardening processes [53,55], the mechanical material behavior can be specified by Young's modulus,

$$E = E_{\text{aus}} \cdot z_{\text{aus}} + E_{\text{mar}} \cdot z_{\text{mar}} + E_{\text{bpf}} \cdot z_{\text{bpf}}, \quad (19)$$

Poisson's ratio,

$$\nu = \nu_{\text{aus}} \cdot z_{\text{aus}} + \nu_{\text{mar}} \cdot z_{\text{mar}} + \nu_{\text{bpf}} \cdot z_{\text{bpf}}, \quad (20)$$

the yield stress,

$$Y = Y_{\text{aus}} \cdot z_{\text{aus}} + Y_{\text{mar}} \cdot z_{\text{mar}} + Y_{\text{bpf}} \cdot z_{\text{bpf}}, \quad (21)$$

and the linear thermal expansion coefficient,

$$\alpha = \alpha_{\text{aus}} \cdot z_{\text{aus}} + \alpha_{\text{mar}} \cdot z_{\text{mar}} + \alpha_{\text{bpf}} \cdot z_{\text{bpf}}. \quad (22)$$

Due to the fact that $E_{\text{aus}} = E_{\text{mar}} = E_{\text{bpf}}$ and $\nu_{\text{aus}} = \nu_{\text{mar}} = \nu_{\text{bpf}}$, it is not necessary to determine E and ν according to Equations (19) and (20). However, this description was chosen as it is also valid for microstructures with differing phase specific properties. In our case, only Y and α differ between the different phases, see Table 2.

As Fillafer et al. [56–59] demonstrated, the mechanical material behavior is not necessarily influenced solely by the amount of the constituting phases and the phase specific material parameters for the pure phases. The arrangement of these phases to each other on grain level, viz. the microstructure, may also have a considerable impact. Due to the simplifications made by using the linear rule of mixture and due to the small plastic deformations occurring during heat treatment (cf. Figure A2d), the assumption of an ideal plastic material behavior appears to be sufficiently accurate.

3. Results and Discussion

3.1. Load Stress Analysis

The results of the load stress analysis for unit cells differing in their geometric parameters are summarized in Figure 7. In each diagram, the maximum of the normalized equivalent stress, $\sigma_{\text{vM}_{\text{max}}}/\sigma_y$, which is defined as the ratio of the maximum v. Mises stress for path 1 (Figure 4) and the loading stress, is shown. The results for the reference geometry listed in Table 1 are highlighted in each diagram.

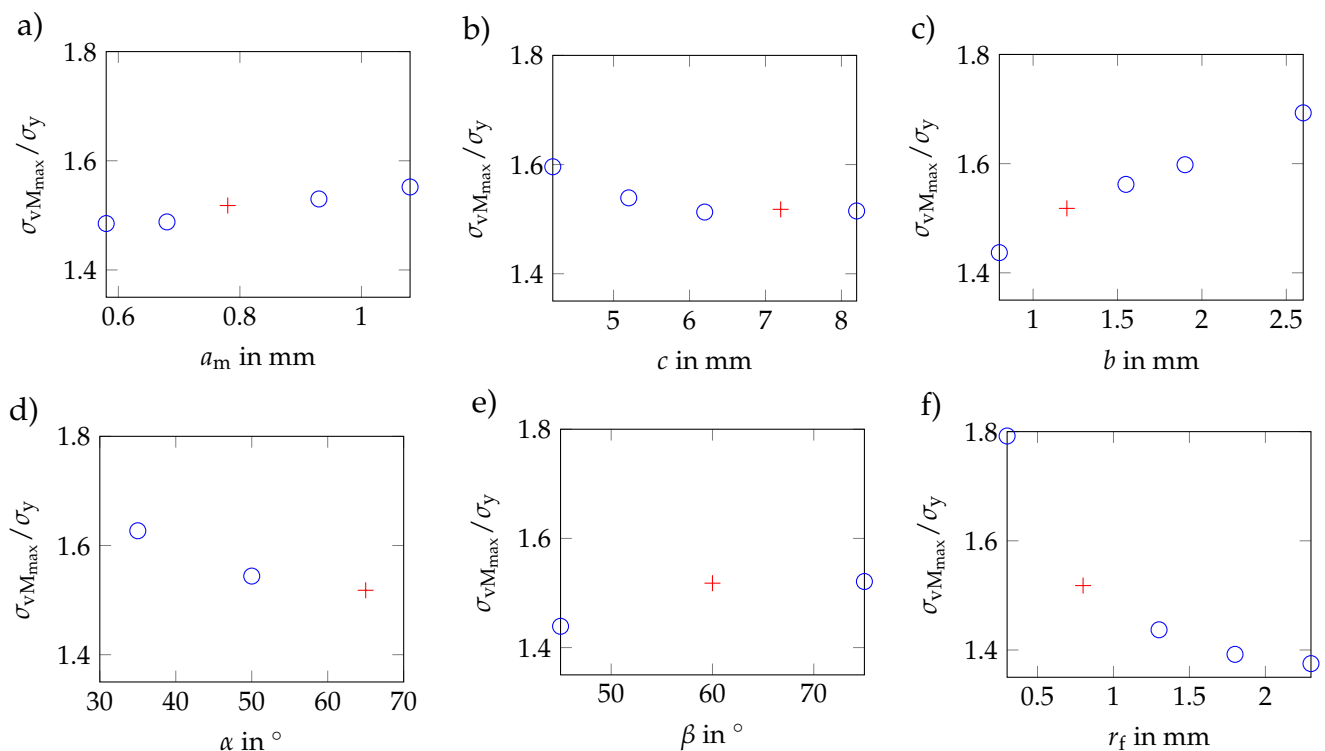


Figure 7. Results of the load-stress analysis (+denotes the reference geometry, see Table 1 and Figure 3): Maximum of the normalized equivalent stress, $\sigma_{\text{vM}_{\text{max}}}/\sigma_y$, along the evaluation path (Figure 4) for different rib heights (a), rib spacings (b), rib widths (c), flank inclinations (d), rib inclinations (e) and foot radii (f).

Figure 7a shows, that $\sigma_{\text{vM}_{\text{max}}}/\sigma_y$ slightly increases with the rib height, a_m . If the rib spacing, c , is lower than the reference value of $c = 7.20$ mm, $\sigma_{\text{vM}_{\text{max}}}/\sigma_y$ increases while larger values for c do not lead to lower peak stresses (Figure 7b). Furthermore, Figure 7c–f indicate, that $\sigma_{\text{vM}_{\text{max}}}/\sigma_y$ rises with increasing rib width, b , decreasing flank inclination, α , increasing rib inclination, β , and decreasing foot radius, r_f . For unit cells with different rib heights, a_m , and rib widths, b , an almost linear dependency between both rib height and rib width and the maximum of the normalized equivalent stress is observed.

For the parameter combinations investigated, $\sigma_{vM_{max}}/\sigma_y$ is influenced strongest by the foot radius, r_f , followed by the rib width, b , which also has a large impact. The impact of flank inclination, rib inclination and rib height is considerably smaller, but still significant. In contrast, the influence of rib spacing is significant only for small values. These results are in good agreement with numerous observations reported in literature [12–16,18–20,24] and extend the current state of knowledge for B500B rebars with small diameters.

These results indicate that it is possible to predict the influence of single geometry parameters on the load stress distribution at least qualitatively with the model geometry used. As a consequence, it is most likely that this is also possible with respect to the thermo-mechanically induced stress concentrations. In comparison with experimental and theoretical investigations, this approach offers the possibility to investigate the influence of single geometry parameters over a wide parameter range for the complex rebar geometry.

3.2. Thermo-Mechanical Analysis

Within the thermo-mechanical analysis, the associated field quantities are predicted for the whole cooling time, $0 \leq t \leq t_2$. The results for the reference geometry (Table 1) subjected to the reference process (Table 4) are presented in Figures 8–10. Figure 8 shows the evolution of temperature and microstructure in the core, the transition zone and at the rebar surface during cooling (see also Figure A2a,b). Figure 9 shows the evolution of the longitudinal residual stress, σ_{yy} , for path 1 (cf. Figure 5). The longitudinal residual stress after complete cooling for path 2 (cf. Figure 5) is shown in Figure 10.

From the results, it can be seen that only a mixture of bainite, pearlite and ferrite is formed in the core of the rebar (Figure 8b), while mostly martensite is formed at the rebar surface (Figure 8c, see also Figure A2b). Lower temperatures at the surface than in the core (Figure 8a) lead to larger shrinkage of the surface region for $t < 0.012$ s. As a consequence, tensile stresses at the surface and compressive stresses in the core develop (Figure 9). For 0.012 s $< t < 0.4$ s, martensite transformation takes place. At $t = 0.4$ s, large compressive stresses at the surface can be reported, as the martensite transformation of the surface regions is associated with a volume expansion and an increasing yield strength. The transformation of bainite, pearlite and ferrite ends at $t \approx 88$ s. As the transformation is accompanied by a volume expansion of the core, compressive stresses at the rebar surface decrease even though the linear thermal expansion of the core is higher than of the martensitic surface region (cf. Table 2). The latter is also true for $t > 88$ s and is the reason for increasing compressive stresses during further cooling.

In Figure 11 the martensite fraction, z_{mar} , the longitudinal residual stress, σ_{yy} , and the tangential residual stress, σ_{xx} , are shown for a rebar with reference geometry, which is subjected to different quenching times, t_1 . The results after complete cooling are evaluated for paths 1 and 3. From the results, it can be seen that the martensite fraction at the rebar surface and the hardening depth increase with increasing quenching time and due to the presence of the rib (Figure 11a,d), because the rebar surface is cooled further below the martensite starting temperature in both cases. Within our modeling framework, this argumentation is plausible as longer quenching times do not affect the heat transfer coefficient and therefore the cooling rate of the rebar surface. As a consequence, the compressive stresses at the rebar surface in longitudinal and tangential directions between two ribs, σ_{yy} , σ_{xx} , increase with increasing quenching time (Figure 11b,c).

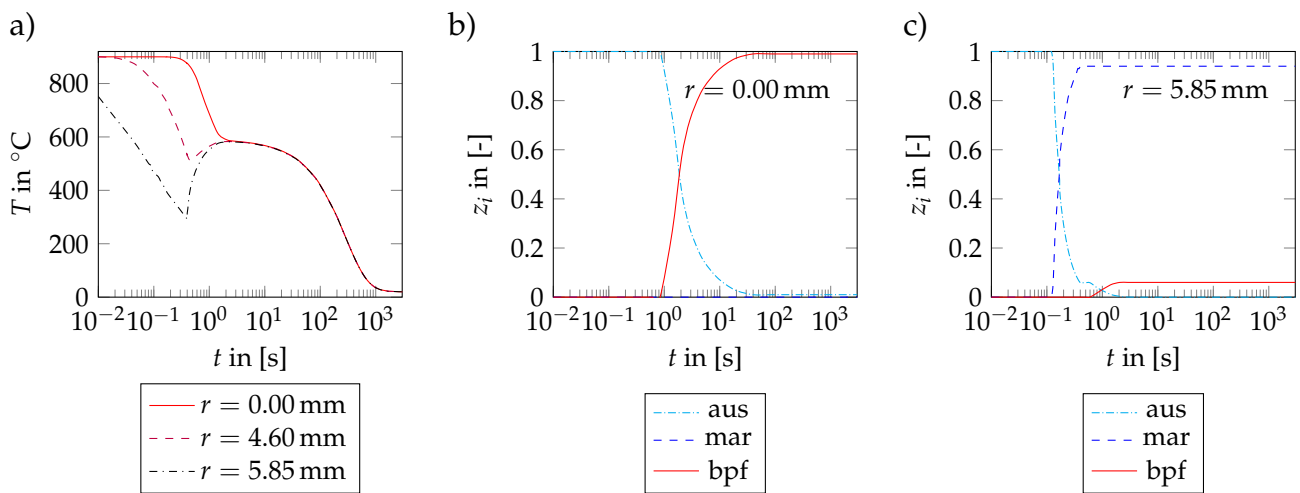


Figure 8. Results of the thermo-mechanical analysis: Evolution of temperature, T , (a) and phase fractions, z_i , (b,c) at selected locations, r , along path 1 (cf. Figure 5) for the rebar with reference geometry according to Table 1 subjected to the reference process (Table 4).

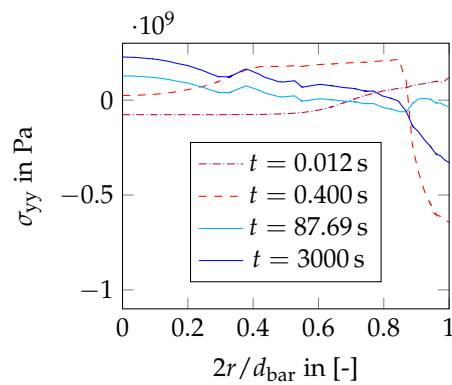


Figure 9. Results of the thermo-mechanical analysis: Longitudinal residual stress, σ_{yy} , along path 1 (cf. Figure 5) for rebars with reference geometry according to Table 1 subjected to the reference process (Table 4) for various times, t .

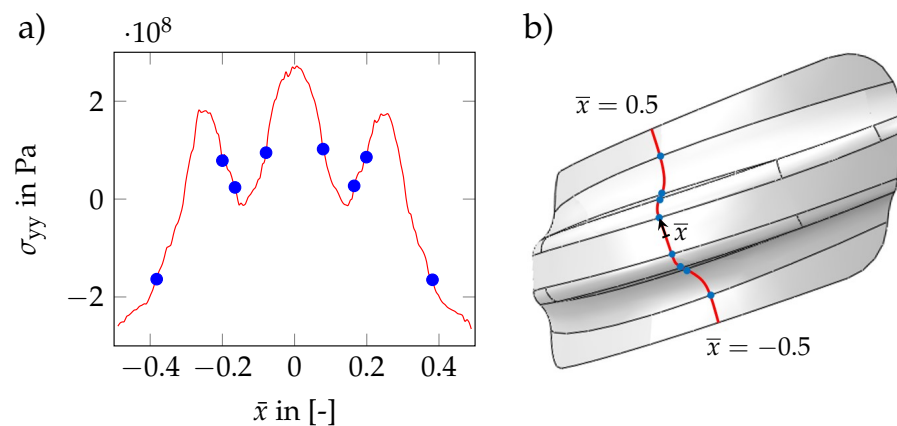


Figure 10. Results of the thermo-mechanical analysis: Longitudinal residual stress, σ_{yy} , as a function of the normalized path variable, \bar{x} , for rebars with reference geometry according to Table 1 subjected to the reference process (Table 4) at $t = t_2$, i.e., after complete cooling (a). Evaluation for path 2 (cf. Figure 5), whereas specific data points associated to the rebar geometry (b) are highlighted in blue.

As for loading stresses in the axial direction (Figure 7), the residual stress level at the rebar surface is strongly influenced by the presence of the rib (Figure 11e,f, see also Figure A2c). While the compressive stress level in the tangential direction is lowered due to the presence of the rib, tensile stresses in the axial direction become evident at the rebar surface. Tensile stresses in the axial direction are highest at the tip of the rib and in the transition zone between the rib and rib radius (Figure 10). In the transition zone of the rib radius and base cylinder, compressive stresses can be predicted.

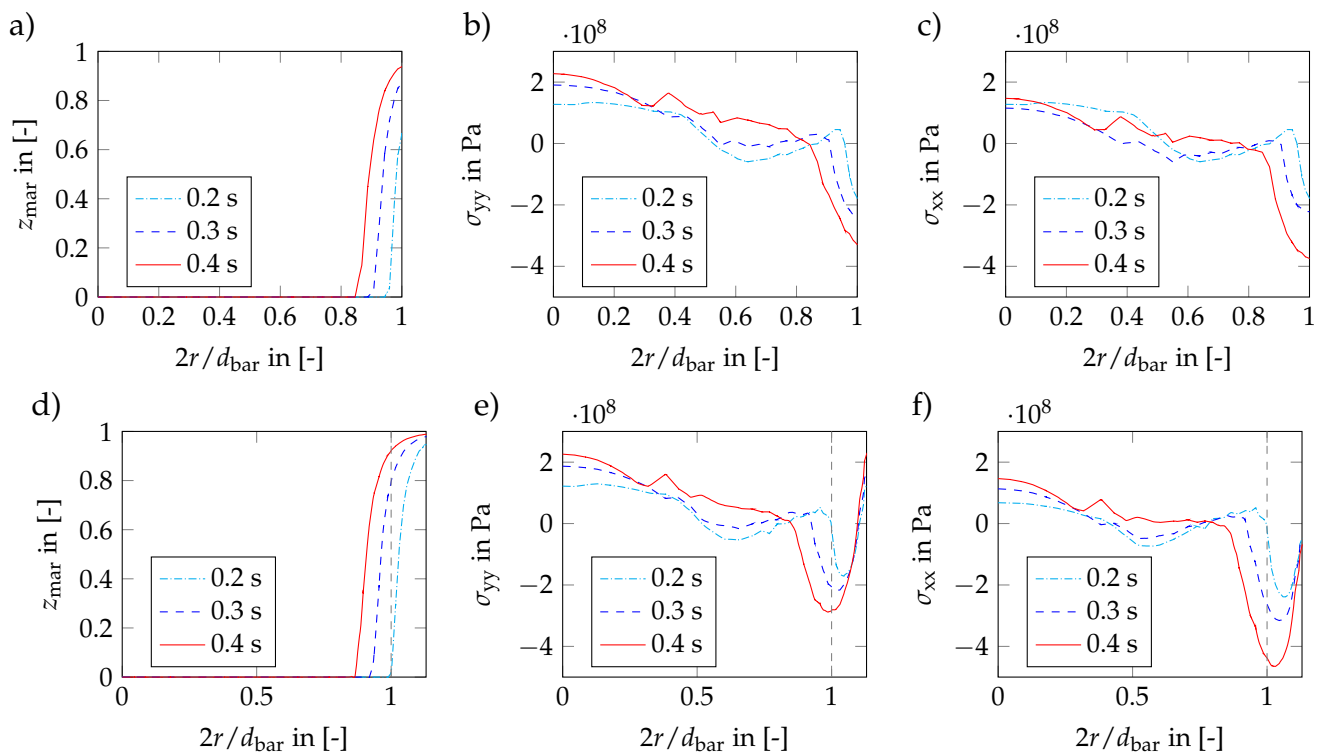


Figure 11. Results of the thermo-mechanical analysis for rebar with reference geometry (Table 1): Martensite fraction (a,d), longitudinal stress (b,e) and tangential stress (c,f) as a function of the normalized radius, $2r/d_{\text{bar}}$, and for different quenching times, t_1 . Evaluation for path 1 (top row) and path 3 (bottom row, cf. Figure 5).

In Table 5, the longitudinal stress, σ_{yy} , is shown for different rebar geometries, which are subjected to the reference process. The rebar geometries vary with regard to individual geometry parameters. The results are evaluated at the end of path 1, i.e., for $r = 5.85$ mm. From the results, it can be seen that the compressive stress level increases for increasing rib height, a_m , decreasing rib spacing, c , and increasing rib width, b . This observation can be related to an increasing cooling effect of the ribs and an increasing hardening depth (cf. Figure 11). For decreasing flank inclination, α , and increasing foot radius, r_f , the residual stress level is nearly unaffected. In both cases, the hardening depth decreases due to an increasing rib volume. As the rib volume increases, however, the amount of transformed martensite in the rib area is obviously about as large as for the reference geometry.

Due to the predicted residual stress distributions, the load stress level in service between two ribs viz. in the transition zone of rib radius and base cylinder, where fatigue cracks usually initiate, should be lowered. As for the load stress analysis, the residual stress level at the rebar surface is increased by increasing rib width, rib height and for small rib spacings. However, an increasing foot radius and a decreasing flank inclination do not lead to a significantly lower stress level.

Table 5. Results of the thermo-mechanical analysis: Longitudinal residual stress, σ_{yy} , for the reference geometry (Table 1) subjected to the reference process (Table 4) as well as for rebars with different rib height, a_m , rib spacing, c , rib width, b , flank inclination, α , and foot radius, r_f . Evaluation at the end of path 1, i.e., for $r = 5.85$ mm, and after complete cooling, i.e., for $t = t_2$.

Symbol	Parameter			Longitudinal Stress		
	Varied Geometry	Reference Geometry	Unit	Varied Geometry	Reference Geometry	Unit
a_m	1.08	0.78	mm	−384		
c	4.20	7.20	mm	−389		
b	2.60	1.20	mm	−352	−329	MPa
α	50	65	°	−323		
r_f	2.30	0.80	mm	−324		

Comparing the computational results of the thermo-mechanical analysis with findings from literature [3,17,18,26,28] leads to the following observations:

- Residual stresses at the rebar surface are reported to have a maximum value of about 150 MPa [3,17,18,28] and are, therefore, lower than predicted by our numerical simulations.
- Findings of experimental investigations regarding the sign of the residual stresses at the rebar surface differ partly from the computational results.

Using the cut compliance technique for rebars with diameters of $d = \{16, 24, 32\}$ mm and parallel transverse ribs, Zheng et al. [17] determined longitudinal compressive residual stresses between -90 and -80 MPa to be present at the rebar surface.

Zubair et al. [3] determined longitudinal and tangential compressive residual stresses of -10 MPa at the rebar surface and of -90 MPa in a depth range of 0.1 to 0.3 mm. These investigations were conducted using X-ray measurements between two alternating transverse ribs utilizing a rebar diameter of $d = 28$ mm.

For rebars with a diameter of $d = 16$ mm, Rocha et al. [18] determined longitudinal compressive residual stresses from -48 to -147 MPa between alternating ribs and from -26 to -61 MPa between parallel ribs using X-ray measurements. However, at a depth of 0.05 mm below the rebar surface, Rocha et al. determined mostly tensile residual stresses of max. 50 MPa. Up to a depth of 2 mm, they measured tensile residual stresses using the cut compliance technique.

Volkwein et al. [28] examined the residual stress distribution in two rebars of the same grade and of identical diameter, $d = 28$ mm, produced from two different manufacturers. Both rebars showed compressive residual stresses in the core of the rebar and tensile residual stresses near the surface. For one of the rebars, compressive residual stresses were determined in a thin surface layer.

4. Conclusions

In this contribution, a modeling approach was presented to examine geometrically and thermo-mechanically induced stress concentrations in ribbed reinforcing bars. In addition to a linear-elastic load stress analysis, a thermo-mechanical analysis of the manufacturing process was conducted.

The results of the load stress analysis agree well with findings reported in literature and extend the current state of knowledge for B500B-rebars with small diameters. For the parameter combinations investigated, the geometrically induced stress concentrations are most influenced by the foot radius of the ribs followed by the rib width, which also has a large impact.

As for the load stress analysis, the residual stress distribution at the rebar surface is strongly influenced by the rib and its geometry. The results of the thermo-mechanical analysis show compressive stresses at the rebar surface between two ribs and tensile stresses in the longitudinal direction at the tip of the rib for all parameter combinations investigated. With increased cooling of the surface region during quenching, the residual stress level

increases in general. This indicates longer quenching times to be favorable with regard to a prolonged service life of ribbed rebars.

Compared to literature data, the predicted residual stress level appears to be high. Regarding the residual stress state at the rebar surface between two ribs, partly contradictory observations can be found in literature. Both tensile and compressive stresses are reported for different rebar samples, while our numerical results predict compressive residual stresses only. The clarification of this discrepancy is the focus of ongoing experimental and numerical investigations.

Author Contributions: Conceptualization, E.W., C.K. and T.R.; software, T.R. and C.H.W.; formal analysis, T.R. and C.H.W.; investigation, T.R.; resources, T.R., C.H.W. and S.R.; writing—original draft preparation, T.R.; writing—review and editing, T.R., C.H.W., E.W. and C.K.; visualization, T.R., C.H.W. and M.Z.S.H.; supervision, E.W. and C.K.; project administration, E.W. and C.K.; funding acquisition, E.W. and C.K. All authors have read and agreed to the published version of the manuscript.

Funding: This research was funded by the Deutsche Forschungsgemeinschaft (DFG, German Research Foundation) under project number 410264412.

Conflicts of Interest: The authors declare no conflict of interest. The funders had no role in the design of the study, in the collection, analysis, or interpretation of data, in the writing of the manuscript, or in the decision to publish the results.

Appendix A. Meshed Models and Selected Results

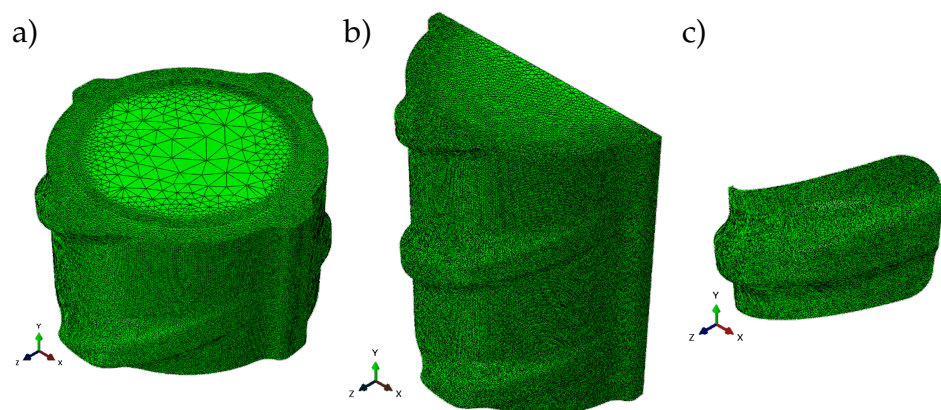


Figure A1. Meshed models (reference geometry, see Table 1) for the load stress (a) and the thermo-mechanical analysis (b,c).

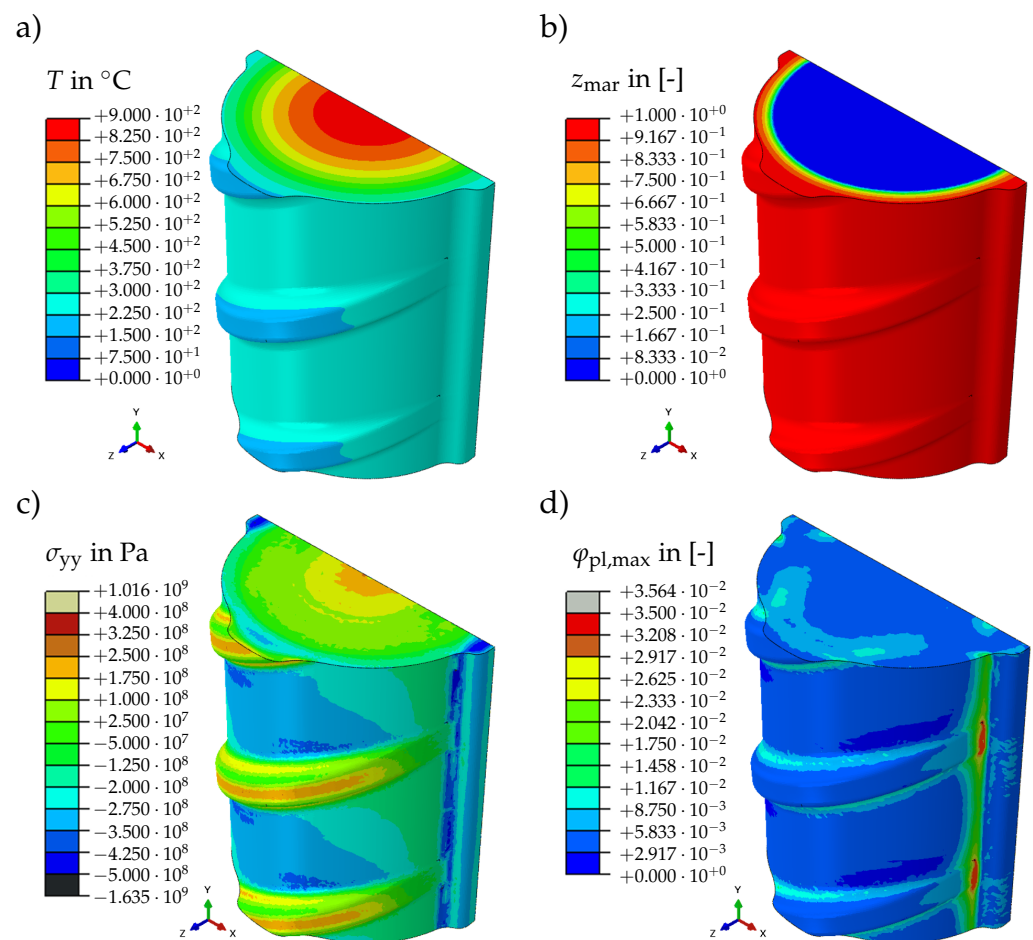


Figure A2. Selected results of the thermo-mechanical analysis for a rebar model with reference geometry (Table 1) subjected to the reference process (Table 4): Temperature, T , at the end of the quenching step, i.e., for $t = t_1$ (a). Martensite fraction z_{mar} (b), longitudinal residual stress σ_{yy} (c) and maximum principal of the plastic strain tensor (d) after complete cooling, i.e., for $t = t_2$.

References

1. DIN-488-1:2009-08; Reinforcing Steels—Part 1: Grades, Properties, Marking. Beuth: Berlin, Germany, 2009.
2. DIN-488-2:2009-08; Reinforcing Steels—Reinforcing Steel Bars. Beuth: Berlin, Germany, 2009.
3. Hameed, M.Z.; Wölfle, C.H.; Robl, T.; Obermayer, T.; Rapp, S.; Osterminski, K.; Krempaszky, C.; Werner, E. Parameter identification for thermo-mechanical constitutive modeling to describe process-induced residual stresses and phase transformations in low-carbon steels. *Appl. Sci.* **2021**, *11*, 550. [CrossRef]
4. Economopoulos, M.; Respen, Y.; Lessel, G.; Steffes, G. Application of the tempcore process to the fabrication of high yield strength concrete-reinforcing bars. *Metall. Rep.* **1975**, *45*, 1–17.
5. Noville, J.F. TEMPCORE, the Most Convenient Process to Produce Low Cost High Strength Rebars from 8 to 75 mm. METEC & 2nd ESTAD, Düsseldorf, Germany, 2015. Available online: https://www.researchgate.net/publication/328530702_TEMPCORE_R_the_most_convenient_process_to_produce_low_cost_high_strength_rebars_from_8_to_75_mm (accessed on 28 October 2021).
6. Goto, Y. Cracks formed in concrete around deformed tension bars. *ACI J.* **1971**, *68*, 244–251.
7. König, G.; Nguyen, V.T.; Kurz, W. *Ein Mechanisches Modell zur Beschreibung des Verbundverhaltens zwischen Stahl und Beton*; Deutsche Forschungsgemeinschaft (DFG); Wiley-VCH: Weinheim, Germany, 2000.
8. Martin, H.; Noakowski, P. *Verbundverhalten von Betonstählen—Untersuchung auf der Grundlage von Ausziehversuchen*; Deutscher Ausschuss für Stahlbeton e.V. (Heft 319); Ernst: Berlin, Germany, 1981.
9. Rehm, G. *Über die Grundlagen des Verbundes zwischen Stahl und Beton*; Deutscher Ausschuss für Stahlbeton e.V. (Heft 138); Ernst: Berlin, Germany, 1961.
10. Rehm, G.; Harre, W.; Beul, W. *Schwingfestigkeitsverhalten von Betonstählen unter wirklichkeitsnahen Beanspruchungs- und Umgebungsbedingungen*; Deutscher Ausschuss für Stahlbeton e.V. (Heft 374); Ernst: Berlin, Germany, 1986.
11. Burton, K.T. Fatigue tests of reinforcing bars. *J. PCA* **1965**, *7*, 13–23.
12. Martin, H.; Schießl, P.; Schwarzkopf, M. *Optimierung der Rippenausbildung hochfester Betonstähle*; Research Report Report Number: Bo 784/83; Institut für Betonstahl und Stahlbetonbau e.V.: Munich, Germany, 1983.

13. Fei, J.; Darwin, D. *Fatigue of High Relative Rib Area Reinforcing Bars*; Research Report (Structural Engineering and Engineering Materials SM Report 54); Federal Highway Administration: Lawrence, KS, USA, 1999.
14. Jhamb, I.C. *Fatigue of Reinforcing Bars*. Ph.D. Thesis, University of Alberta, Edmonton, AB, Canada, 1972.
15. Helgason, T.; Hanson, J.; Somes, N.; Corley, W.; Hognestad, E. *Fatigue Strength of High-Yield Reinforcing Bars*; Research Report (National Cooperative Highway Research Program, Report Number: 164); National Research Council: Washington, DC, USA, 1976.
16. Zheng, H.; Abel, A. Stress concentration and fatigue of profiled reinforcing bars. *Int. J. Fatigue* **1998**, *20*, 767–773. [[CrossRef](#)]
17. Zheng, H.; Abel, A. Fatigue properties of reinforcing steel produced by TEMP CORE process. *J. Mater. Civ. Eng.* **1999**, *11*, 158–165. [[CrossRef](#)]
18. Rocha, M.; Brühwiler, E.; Nussbaumer, A. Geometrical and material characterization of quenched and self-tempered steel reinforcement bars. *J. Mater. Civ. Eng.* **2016**, *28*, 04016012-1. [[CrossRef](#)]
19. Martin, H.; Schießl, P. *Dauerschwingfestigkeit von unbehandelten Betonstählen—Zusammenfassender Überblick über Versuchsergebnisse und theoretische Erkenntnisse*; Research Report (Report Number: Sch/K-105/75); Institut für Betonstahl und Stahlbetonbau e.V.: Munich, Germany, 1975.
20. Majumdar, S.; Ali, R.; Kumar, A.; Deb, A. Optimum rib design in TMT rebars to enhance fatigue life while retaining bond strength. *J. Mater. Civ. Eng.* **2018**, *3*, 04017313. [[CrossRef](#)]
21. Gehlen, C.; Osterminski, K.; Weirich, T. High-cycle fatigue behaviour of reinforcing steel under the effect of ongoing corrosion. *Struct. Concr.* **2016**, *17*, 329–337. [[CrossRef](#)]
22. Hanson, J.M.; Burton, K.T.; Hognestad, E. Fatigue tests of reinforcing bars—Effect of deformation pattern. *J. PCA* **1969**, *10*, 2–13.
23. MacGregor, J.G.; Jhamb, I.C.; Nutall, N. Fatigue strength of hot-rolled reinforcing bars. *ACI J.* **1971**, *68*, 169–179.
24. Martin, H.; Schießl, P. *Untersuchungen zur Dauerschwingfestigkeit von dispersionsgehärteten Betonrippenstählen BSt50/55 mit III U- und IV U-Profilierung*; Research Report (Report Number: 18574); Institut für Betonstahl und Stahlbetonbau e.V.: Munich, Germany, 1974.
25. Scholz, M. *Untersuchungen zum Einfluss der Eigenspannungen auf das Dauerschwingverhalten von Betonstahl*. Master's Thesis, Technical University of Munich, Munich, Germany, 2016.
26. Liscic, B.; Tensi, H.M.; Luty, W. *Theory and Technology of Quenching*; Springer: Berlin, Germany, 1992.
27. Suzuki, H.; Kusunoki, K.; Hatanaka, Y.; Mukai, T.; Tasai, A.; Kanematsu, M.; Kabayama, K.; Harjo, S. Measuring strain and stress distributions along rebar embedded in concrete using time-of-flight neutron diffraction. *Meas. Sci. Technol.* **2014**, *25*, 025602. [[CrossRef](#)]
28. Volkwein, A.; Osterminski, K.; Meyer, F.; Gehlen, C. Distribution of residual stresses in reinforcing steel bars. *Eng. Struct.* **2020**, *223*, 111140. [[CrossRef](#)]
29. Cetinel, H.; Toparli, M.; Özsoyeller, L. A finite element based prediction of the microstructural evolution of steels subjected to the Tempcore process. *Mech. Mater.* **2000**, *32*, 339–347. [[CrossRef](#)]
30. Bandyopadhyay, K.; Lee, J.; Shim, J.-H.; Hwang, B.; Lee, M.-G. Modeling and experiment on microstructure evolutions and mechanical properties in grade 600 MPa reinforcing steel rebar subjected to TempCore process. *Mater. Sci. Eng. A* **2019**, *745*, 39–52. [[CrossRef](#)]
31. Hosny, S.; Gepreel, M.A.H.; Ibrahim, M.G.; Bassuony, A.R. Simulation of Tempcore process for 500 MPa steel bars. *Met. Mater. Int.* **2020**, *27*, 3359–3370. [[CrossRef](#)]
32. Khalifa, H.; Megahed, G.M.; Hamouda, R.M.; Taha, M.A. Experimental investigation and simulation of structure and tensile properties of Tempcore treated rebar. *J. Mater. Process. Technol.* **2016**, *230*, 244–253. [[CrossRef](#)]
33. Park, C.S.; Yi, H.J.; Kim, Y.T.; Han, S.W.; Lee, T.; Moon, Y.H. Tempcore process simulator to analyze microstructural evolution of quenched and tempered rebar. *Appl. Sci.* **2019**, *9*, 2938. [[CrossRef](#)]
34. Dimatteo, A.; Vannucci, M.; Colla, V. A finite element method for the prediction of thermal, metallurgical, and mechanical behavior of rebars in the TempCore process. *Steel Res. Int.* **2015**, *87*, 276–287. [[CrossRef](#)]
35. Park, C.S.; van Tyne, C.J.; Lee, S.J.; Lee, T.; Kim, J.H.; Moon, Y.H. Prediction of Tempcore rebar strength using a thermomechanical simulator with a designed hollow specimen. *Steel Res. Int.* **2020**, *91*, 1900520. [[CrossRef](#)]
36. Akbarpour, M.R.; Mashhuriazar, A.; Daryani, M. Experimental and numerical investigation on the effect of the Tempcore process parameters on microstructural evolution and mechanical properties of dual phase steel reinforcing rebars. *Met. Mater. Int.* **2020**, *27*, 4074–4083. [[CrossRef](#)]
37. Smith, M. *ABAQUS/Standard User's Manual*; Dassault Systemes Simulia Corp.: Johnston, RI, USA, 2014.
38. *DIN EN ISO 17660-1:2006*; *Welding—Welding of Reinforcing Steel—Part 1: Load-Bearing Welded Joints*. Beuth: Berlin, Germany, 2006.
39. Dassault Systemes Solid Works Corp. *Solid Works*; Dassault Systemes Solid Works Corp.: Waltham, MA, USA, 2019.
40. Wölfle, C.; Kremaszky, C.; Werner, E. An implicit integration scheme with consistent tangent modulus for Leblond's model of transformation induced plasticity in steels. *Contin. Mech. Thermodyn.* **2022**, *34*, 321–340. [[CrossRef](#)]
41. Leblond, J.B.; Mottet, G.; Devaux, J.C. A theoretical and numerical approach to the plastic behaviour of steels during phase transformations—II. Study of classical plasticity for ideal-plastic phases. *J. Mech. Phys. Solids* **1986**, *34*, 411–432. [[CrossRef](#)]
42. Cadoni, E.; Fontana, M.; Forni, D.; Knobloch, M. High strain rates testing and constitutive modeling of B500B reinforcing steel at elevated temperatures. *Eur. Phys. J. Special Topics* **2018**, *22*, 179–199. [[CrossRef](#)]

43. Matplus GmbH. *JMatPro*; Matplus GmbH: Wuppertal, Germany, 2021.
44. Kreith, F.; Black, W.Z. *Basic Heat Transfer*; Harper and Row Publishers: New York, NY, USA, 1980.
45. Sankar, I.B.; Rao, K.M.; Krishna, A.G. Prediction of heat transfer coefficient of steel bars subjected to Tempcore process using nonlinear modeling. *Int. J. Adv. Manuf. Technol.* **2010**, *47*, 1159–1166. [[CrossRef](#)]
46. Koistinen, D.P.; Marburger, R.E. A general equation prescribing the extent of the austenite–martensite transformation in pure iron–carbon alloys and plain carbon steels. *Acta Metall.* **1959**, *7*, 59–60. [[CrossRef](#)]
47. Kolmogorov, A.N. On the statistical theory of the crystallization of metals. *Bull. Acad. Sci. USSR Math. Ser.* **1937**, *1*, 355–359.
48. Johnson, W.A.; Mehl, R.F. Reaction kinetics in processes of nucleation and growth. *Trans. Am. Inst. Min. Metall. Eng.* **1939**, *135*, 416–442.
49. Avrami, M. Kinetics of phase change. I General Theory. *J. Chem. Phys.* **1939**, *7*, 1103–1112. [[CrossRef](#)]
50. Avrami, M. Kinetics of phase change. II Transformation-time relations for random distribution of nuclei. *J. Chem. Phys.* **1940**, *8*, 212–224. [[CrossRef](#)]
51. Scheil, E. Anlaufzeit der Austenitumwandlung. *Arch. Eisenhüttenwesen* **1935**, *8*, 565–567. [[CrossRef](#)]
52. Henderson, D.W. Thermal analysis of non-isothermal crystallization kinetics in glass forming liquids. *J. Non-Cryst. Solids* **1979**, *30*, 301–315. [[CrossRef](#)]
53. Simsir, C.; Gür, C.H. 3D FEM simulation of steel quenching and investigation of the effect of asymmetric geometry on residual stress distribution. *J. Mater. Process. Technol.* **2008**, *207*, 211–221. [[CrossRef](#)]
54. Lippmann, H. *Mechanik des plastischen Fließens*; Springer: Berlin, Germany, 1981.
55. Gür, C.H.; Tekkaya, A.E. Finite element simulation of quench hardening. *Steel Res. Int.* **1996**, *67*, 298–306. [[CrossRef](#)]
56. Fillafer, A. Fließ- und Mikroschädigungsverhalten ferritisch-martensitischer Dualphasenstähle. Ph.D. Thesis, Technical University of Munich, Munich, Germany, 2017.
57. Fillafer, A.; Kremaszky, C.; Werner, E. On strain partitioning and micro-damage behavior of dual-phase steels. *Mater. Sci. Eng. A* **2014**, *614*, 180–192. [[CrossRef](#)]
58. Fillafer, A.; Werner, E.; Kremaszky, C. On phase transformation induced effects controlling the initial flow behavior of ferritic-martensitic dual-phase steels. *Mater. Sci. Eng. A* **2017**, *708*, 556–562. [[CrossRef](#)]
59. Robl, T.; Kremaszky, C.; Fillafer, A.; Werner, E. Examining the unloading behavior of dual-phase steels by means of microstructure simulations. *Mater. Sci. Eng. A* **2021**, *823*, 141744. [[CrossRef](#)]